Chinese Journal of
POLYMER SCIENCE

RESEARCH ARTICLE

https://doi.org/10.1007/s10118-026-3880-6
Chinese J. Polym. Sci.

Cryo-induced Encapsulation of Amino-functionalized Zeolitic Imidazolate Framework-8 Microspheres within Biomass-based Cryogel Walls for Effective Hemoperfusion

Pei-Rong Jiang[a], Xu-Feng Zhang[a*], Ji-Ping Weng[a], Yan Liu[b], Jin Huang[b*], Xiang-Yu Chen[c*], Jing Shen[a*], Xi-Yun Feng[a], Liang-Fei Duan[a], and Jun Wang[a]

[a] *Yunnan Key Laboratory of Modern Separation Analysis and Substance Transformation, College of Chemistry and Chemical Engineering, Yunnan Normal University, Kunming 650500, China*
[b] *School of Chemistry and Chemical Engineering, Shihezi University, Shihezi 832003, China*
[c] *Emergency Department, Southwest Hospital of Army Medical University, Chongqing 400038, China*

Electronic Supplementary Information

Abstract Efficient removal of protein-bound toxins remains a formidable challenge in artificial liver support systems because of the persistent trade-off between adsorption capacity and hemocompatibility. In this study, a wall-integrated cryogel was developed by embedding amino-functionalized zeolitic imidazolate framework-8 (mZIF-8) within a biomass matrix of quaternized chitosan (QCS) and microfibrillated cellulose (MFC) using a green cryo-induced assembly process. During freezing, the mZIF-8 nanoparticles were concentrated in the polymer-rich interstitial regions and assembled into microspheres that became confined within the cryogel walls, resulting in a microsphere-in-wall architecture. The optimized mZIF-8@QCS/MFC cryogel showed a bilirubin saturation capacity of 146.6 mg/g in albumin-containing solution. Spectroscopic analysis suggested that bilirubin capture involved the combined contribution of electrostatic attraction from the positively charged polysaccharide matrix and the hydrogen bonding provided by mZIF-8. The hydrophilic biomass walls reduced the direct exposure of mZIF-8 to the external environment and limited nonspecific albumin adsorption. The composite cryogel exhibited a hemolysis ratio of 0.4% and stable performance under continuous-flow conditions. These results show that spatial regulation of metal-organic frameworks (MOFs) locations within carbohydrate cryogel walls may provide a useful strategy for balancing adsorption accessibility and blood-contacting compatibility in the design of bilirubin adsorbents.

Keywords Bilirubin adsorption; Polysaccharide cryogel; Microsphere-in-wall architecture; Hemoperfusion

Citation: Jiang, P. R.; Zhang, X. F.; Weng, J. P.; Liu, Y.; Huang, J.; Chen, X. Y.; Shen, J.; Feng, X. Y.; Duan, L. F.; Wang, J. Cryo-induced encapsulation of amino-functionalized zeolitic imidazolate framework-8 microspheres within biomass-based cryogel walls for effective hemoperfusion. *Chinese J. Polym. Sci.* https://doi.org/10.1007/s10118-026-3880-6

INTRODUCTION

Extracorporeal blood purification has evolved from simple diffusion-based clearance toward adsorption-based strategies for the removal of toxins that are difficult to eliminate by hemodialysis.[1,2] Among these toxins, bilirubin is of particular concern in liver failure,[3,4] as its accumulation is closely associated with poor prognosis and severe systemic complications.[5–7] Unlike small and water-soluble metabolites that are efficiently cleared by hemodialysis, these hydrophobic toxins circulate tightly bound to serum albumin.[8–10] This binding creates a bulky complex that cannot permeate dialysis membranes,[11,12] leading to persistent toxin accumulation. This creates a strong need for adsorbent materials that can selectively capture bilirubin by competing with albumin.[13]

Hemoperfusion is considered a promising approach for removing albumin-bound bilirubin because it allows direct contact between the blood and sorbent materials.[14,15] Conventional adsorbents, such as activated carbon and polymeric resins, have been used clinically, but they often suffer from insufficient selectivity and unsatisfactory blood compatibility.[16–18] Recently, metal-organic frameworks (MOFs) have garnered considerable interest for adsorption and separation because of their high surface area, tunable pore structures, and adjustable chemical functionality.[19,20] Zeolitic imidazolate framework-8 (ZIF-8) is a representative framework with high structural stability and facile synthesis.

* Corresponding authors, E-mail: xfzhang@ynnu.edu.cn (X.F.Z.)
E-mail: huangjin@iccas.ac.cn (J.H.)
E-mail: xiangyuchen@tmmu.edu.cn (X.Y.C.)
E-mail: shenjing@ynnu.edu.cn (J.S.)
Special Topic: Non-Food Biomass Materials
Received July 7, 2026; Accepted September 7, 2026; Published online November 9, 2026

© Chinese Chemical Society
Institute of Chemistry, Chinese Academy of Sciences

The adsorption behavior can be further tailored by ligand functionalization. Notably, amino-containing groups are favorable for bilirubin capture because they can provide electrostatic interactions and hydrogen bonding sites.[14,21–23]

Although functionalized MOFs show potential for bilirubin adsorption, their direct use in hemoperfusion remains limited by their biosafety. To improve handling and avoid particle dispersion, MOFs are often incorporated into beads,[24] hydrogels,[25] or aerogels.[26] However, these approaches typically involve structural tradeoffs. Dense polymer encapsulation improves particle retention and minimizes direct blood contact; however, it may hinder mass transfer and limit bilirubin access to internal adsorption sites. Conversely, increased MOF exposure may enhance the number of adsorption sites at the expense of particle leakage, hemolysis, and protein fouling. Therefore, the key challenge lies in designing an architecture in which MOF particles are securely immobilized within the matrix, while remaining accessible to bilirubin. Natural biomass cryogels, particularly those based on polysaccharides, provide an attractive matrix for hemoperfusion owing to their interconnected macroporous networks, low flow resistance, and excellent biocompatibility. However, blending MOF nanoparticles into polysaccharide-based cryogels often faces challenges in preserving polysaccharide biocompatibility and utilizing the active sites of the MOF particles.

To overcome these limitations, we envisioned that the cryo-concentration effect associated with freeze-induced crosslinking could be harnessed to dictate the spatial organization of MOFs within a macroscopic polysaccharide network, thereby constructing a functionally segregated microsphere-in-wall architecture. Conceptually, ice crystal growth concentrates the dispersed MOF nanoparticles and polysaccharide chains within unfrozen interstitial microphases, promoting the *in situ* self-assembly of MOFs into densely packed microspheres while simultaneously entrapping them within the crosslinked polysaccharide walls. Ideally, this unique structural configuration would help alleviate the trade-off between the adsorption capacity and hemocompatibility. The interconnected macroporous network facilitates rapid perfusion, the wall-confined MOF microspheres serve as sites for bilirubin capture, and the highly hydrophilic polysaccharide matrix acts as a robust hydration barrier to reduce nonspecific protein fouling and direct damage to the blood cells.

Guided by this rational design, we developed a cryo-induced wall-integrated mZIF-8@QCS/MFC cryogel using quaternized chitosan (QCS) and microfibrillated cellulose (MFC) as biomass materials, with excellent hemocompatibility for bilirubin hemoperfusion. Amino-functionalized ZIF-8 (mZIF-8) nanoparticles were first prepared *via* a mixed-ligand strategy using histamine as the functional ligand. During freezing, the assembly and simultaneous confinement of the mZIF-8 microspheres within the QCS/MFC walls were successfully achieved. The resulting cryogel exhibited a maximum adsorption capacity of 146.6 mg/g, low hemolysis, and good stability under dynamic flow conditions. These results suggest that wall-integrated encapsulation may be a useful structural strategy for improving the stability and adsorption performance of MOF-based adsorbents in hemoperfusion applications.

MATERIALS AND METHODS

Materials

Microfibrillated cellulose (MFC) suspensions with a solid content of 2 wt% were purchased from Guilin Qihong Technology Co., Ltd. (Guangxi, China). The fibers had diameters of 0.1–1.0 μm and lengths above 20 μm. Quaternized chitosan (QCS) with a quaternization degree of 98.5% and viscosity of 68.79 mPa·s (1% aqueous solution, 20 °C) was obtained from Macklin Bio-Chem Technology Co., Ltd. (Shandong, China). Bilirubin was obtained from Energy Chemical Reagents Co., Ltd. (Anhui, China). Bovine serum albumin (BSA), bis(vinylsulfonyl)methane (BVSM), HCl, $ZnCl_2$, 2-methylimidazole, histamine dihydrochloride, and NaOH were supplied by the Xiya Reagent (Shandong, China). NaCl, KCl, $Na_2HPO_4{\cdot}12H_2O$, and KH_2PO_4 were purchased from Tianjin Zhiyuan Chemical Reagent Co., Ltd. (Tianjin, China). Coagulation test kits were obtained from Mantino Medical Devices Co., Ltd. (Changchun, China). All chemicals were of analytical grade and were used as received without further purification.

Synthesis of mZIF-8

A mixed-ligand strategy was used to prepare the mZIF-8. First, 2-methylimidazole (0.9853 g, 12 mmol) was dissolved in a mixture of deionized water (21 mL) and methanol (9 mL). Histamine dihydrochloride (0.7363 g, 4 mmol) was added as a functional ligand to introduce amino groups into the framework. After complete dissolution, $ZnCl_2$ (0.2726 g, 2 mmol) was added as a metal precursor. The pH of the reaction solution was adjusted to 8.0, using a NaOH solution. The mixture was stirred at room temperature for 6 h and aged without disturbance for 12 h. The resulting product was collected *via* centrifugation, washed several times with deionized water, and freeze-dried to obtain a white powder.

Preparation of mZIF-8@QCS/MFC Cryogels

The mZIF-8@QCS/MFC composite cryogels were prepared by cryo-induced chemical crosslinking, with minor modifications based on a previous report.[27] Briefly, 0.30 g of QCS was added to 10 g of the MFC suspension with a solid content of 2.0 wt%, followed by the addition of 10 mL of distilled water. The mixture was stirred at 500 r/min for 120 min until homogeneous dispersion was obtained. Predetermined amounts of mZIF-8 nanoparticles were then gradually introduced into the suspension, followed by stirring at 500 r/min for 60 min to ensure a uniform dispersion. Subsequently, 0.60 g of BVSM was added as a crosslinker and stirred at 500 r/min for 3 min. The resulting mixture was immediately transferred to plastic syringes and frozen at −13 °C for 12 h. After thawing at room temperature, the cryogels were thoroughly washed with deionized water to remove any unreacted species. The samples were then subjected to solvent exchange with ethanol and air-dried at 25 °C. The dried cryogels retained their original macroscopic shape without any obvious shrinkage and were used for subsequent characterization.

For comparison, cryogels prepared with different mZIF-8 loadings were denoted as mZIF-8@QCS/MFC-*x*, where *x* represents the mass of mZIF-8 in milligrams. For example, mZIF-8@QCS/MFC-15 refers to a sample containing 15 mg of mZIF-8. Pristine QCS/MFC cryogel was prepared using the same procedure without the addition of mZIF-8.

https://doi.org/10.1007/s10118-026-3880-6

Characterization

The mechanical properties and shape recovery of the cryogels were tested using a universal testing machine (UTM-2502; SUNS Technology, China) at a compression rate of 3 mm/min. The morphology of the mZIF-8@QCS/MFC-15 cryogel was examined using scanning electron microscopy (SEM, Zeiss Sigma 300, Germany) to analyze the macroporous size distribution and particle embedding. Fourier transform infrared spectroscopy (FTIR; Bruker Corporation MPA, Germany) was used to investigate the functional groups present in the cryogels. X-ray photoelectron spectroscopy (XPS, Thermo Scientific K-Alpha, USA) was used for surface elemental composition analysis. The thermal stability and degradation behavior of the cryogels were examined using thermogravimetric analysis (TGA, SDT-650, Germany). The surface area, pore volume, and average pore width of the cryogels were determined from N_2 adsorption/desorption isotherms using a gas adsorption analyzer (Micromeritics ASAP 2460, USA) after degassing at 80 °C for 12 h.

Biocompatibility Assessment

Hemolysis test

The hemolysis test was performed in accordance with relevant ethical requirements. The cryogel samples were first equilibrated in phosphate-buffered saline for 30 min. After removing the washing solution, 10 mL of fresh PBS was added to each sample. PBS and distilled water were used as negative and positive controls, respectively. All groups were pre-incubated at 37 °C for 30 min. Then, 0.2 mL of diluted sterile porcine blood was added to each tube and incubated at 37 °C for another 60 min. After centrifugation at 1500 r/min for 12 min, the absorbance of the supernatant was measured at 545 nm. The hemolysis ratio was calculated using Eq. (1).

$$\text{Hemolysis ratio}\,(\%) = \frac{A_s - A_n}{A_p - A_n} \times 100 \quad (1)$$

where A_s, A_n, and A_p represent the absorbance of the sample, the negative control, and the positive control, respectively.

Anticoagulation test

To evaluate the effect of cryogels on the coagulation system, the activated partial thromboplastin time (APTT), prothrombin time (PT), and thrombin time (TT) were measured. Cryogel samples (10 mg) were immersed in PBS overnight and incubated at 37 °C for 1 h. After removal of the PBS, 5 mL of fresh sterile porcine blood was added and incubated at 37 °C for 3 h. The cryogels were then removed and plasma was collected by centrifugation. Coagulation parameters were analyzed using a semi-automatic coagulation analyzer (MTN-II, Mantino Medical Devices Co., Ltd., China).

Cytotoxicity test

The cytotoxicity of the cryogels was assessed using a Cell Counting Kit-8 assay. Sterilized cryogel samples were immersed in a cell culture medium to prepare sample extracts. Human umbilical vein endothelial cells in the logarithmic growth phase were seeded into 96-well plates at a density of 8×10^3 cells per well and cultured overnight at 37 °C in a humidified atmosphere containing 5% CO_2. The medium was then replaced with 100 μL of fresh culture medium for the control group or extract-containing medium for the experimental group. Each condition was tested in triplicates. After incubation for 24 h, the medium was removed and the cells were washed three times with PBS. Subsequently, 100 μL of the culture medium containing 10% CCK-8 reagent was added to each well. After 2 h of incubation, absorbance was measured at 450 nm using a microplate reader. The cell viability was calculated using Eq. (2).

$$\text{Cell viability}\ (\%) = \frac{A_{\text{test}} - A_0}{A_{\text{control}} - A_0} \times 100 \quad (2)$$

where A_{test}, A_0, and A_{control} represent the absorbance values of the experimental, blank, and control groups, respectively. Each sample was replicated three times, and the average value was used.

Batch Adsorption

Batch adsorption experiments were conducted to determine the kinetics and isotherms, which are detailed in the electronic supplementary information (ESI).

Simulated Hemoperfusion

Continuous-flow adsorption was evaluated using a simulated hemoperfusion setup comprising a peristaltic pump and plastic columns packed with mZIF-8@QCS/MFC-15 cryogels of different lengths. An albumin-bound bilirubin solution with an initial bilirubin concentration of 200 mg/L was pumped through the column at the selected flow rates. Effluent samples were collected every 2 min and analyzed for residual bilirubin concentration until the breakthrough approached saturation. The breakthrough curves were fitted using the Thomas and Yoon-Nelson models, as described in ESI.

RESULTS AND DISCUSSION

Synthesis and Characterization of mZIF-8

To improve the affinity of ZIF-8 toward bilirubin, mZIF-8 was synthesized using a mixed-ligand strategy, in which histamine was introduced together with 2-methylimidazole during framework formation (Fig. 1a). The purpose of this design was to incorporate additional amino groups while maintaining the crystalline structure of ZIF-8,[28] thereby providing more favorable interaction sites for bilirubin adsorption.

As depicted in Fig. S1 (in ESI), SEM observations showed that the obtained mZIF-8 particles retained the typical rhombic dodecahedral morphology of ZIF-8 and exhibited a relatively uniform particle size distribution.[29] Elemental mapping further confirmed the homogeneous distribution of C, N, O, and Zn throughout the particles, indicating successful incorporation of the constituent elements within the framework (Fig. S2 in ESI). The crystallographic structure of mZIF-8 was examined using XRD. As shown in Fig. S3 (in ESI), the diffraction pattern of mZIF-8 matches well with the simulated pattern of ZIF-8, and no obvious impurity peaks are detected.[30] This result suggests that the introduction of histamine did not disrupt the overall framework topology. The presence of amino groups was further verified using FTIR and XPS analyses. The FTIR spectrum (Fig. S4 in ESI), a broad absorption band appeared at approximately 3600 cm^{-1}, which can be assigned to N—H stretching vibrations.[31] The XPS profiles (Fig. S5 in ESI), the N 1s region could be deconvoluted into two components centered at 399.02 and 400.0 eV,[32,33] corresponding to the imidazole nitrogen and primary amine groups, respectively. The Zn 2p signals remained consistent with the Zn—N coordination environment of ZIF-8, indicating that the metal-ligand coordination structure was

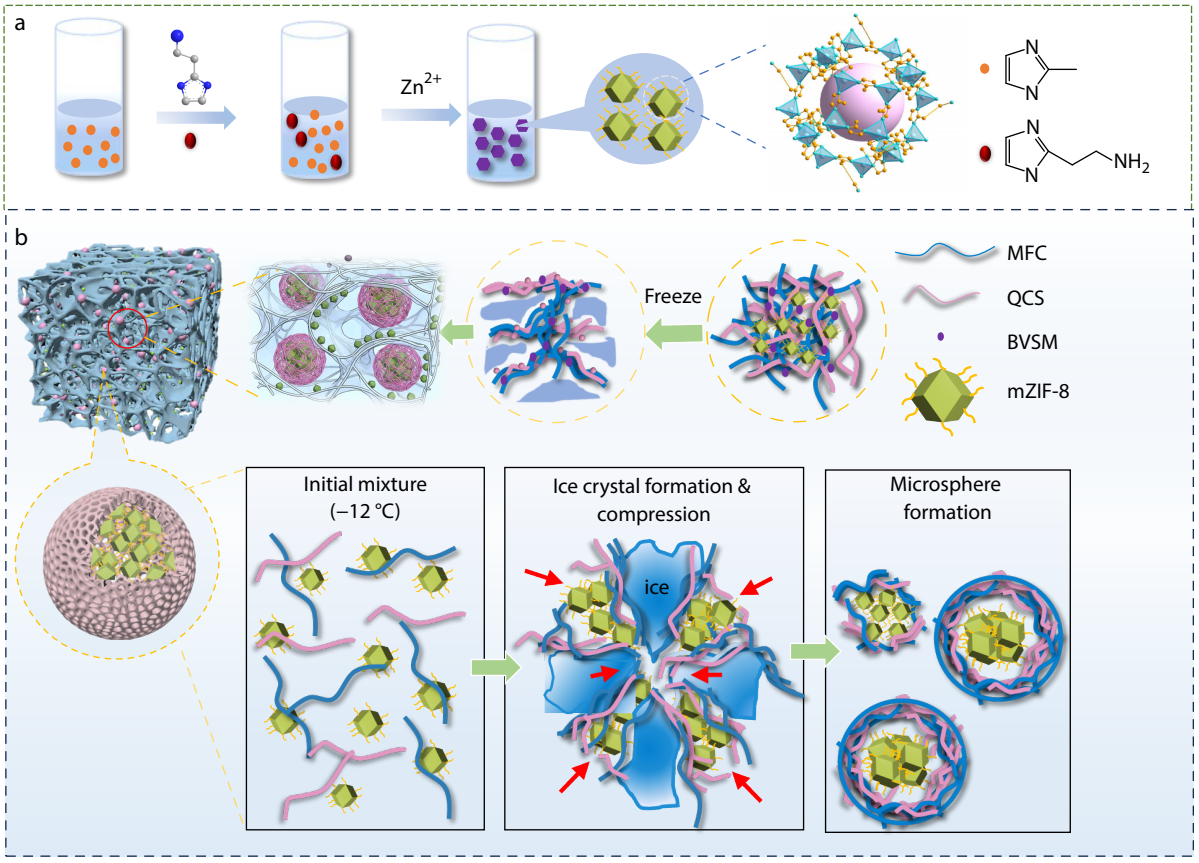


Fig. 1 Schematic illustration of the preparation of the wall-integrated mZIF-8@QCS/MFC cryogel. (a) Mixed-ligand synthesis of amino-functionalized mZIF-8 using 2-methylimidazole and histamine; (b) Fabrication of the mZIF-8@QCS/MFC cryogel through cryo-induced assembly, where mZIF-8 nanoparticles are concentrated in the polymer-rich regions during freezing and confined within the QCS/MFC cryogel walls after crosslinking.

preserved after ligand modification. N_2 adsorption-desorption analysis (Fig. S6 in ESI) showed that the BET surface area decreased slightly from 1006 m^2/g to 904 m^2/g after amino functionalization, which is reasonable considering the partial occupation of the pores by the introduced ligand. Simultaneously, the average pore size increased from 1.33 nm to 1.82 nm. This suggests that the incorporation of histamine may have affected the local pore environment and generated a somewhat more open structure for guest diffusion.[28] These results indicate that mZIF-8 was successfully prepared with preserved crystallinity and modified surface chemistry suitable for bilirubin adsorption. To verify the role of amino functionalization, we compared the bilirubin uptake of cryogels loaded with pristine ZIF-8 and mZIF-8 under the same conditions. As shown in Fig. S7 (in ESI), the mZIF-8-based cryogel exhibited markedly higher adsorption capacity. These results clearly demonstrate that the introduction of amine groups *via* histamine provides additional binding sites, enhancing the specific affinity for albumin-bound bilirubin.

Architecture of the Wall-integrated mZIF-8@QCS/MFC Cryogels

To translate the mZIF-8 powder into a macroscopic hemoperfusion adsorbent, we implemented a cryo-induced wall-integration strategy and proposed a corresponding formation mechanism to engineer a hierarchical microsphere-in-wall architecture (Fig. 1b). During freezing, the advancing ice front is expected to generate ice-rich regions that subsequently develop into macropores while concentrating mZIF-8 nanoparticles and QCS/MFC polysaccharides into a highly compressed interstitial state. This cryo-concentration effect may promote the local accumulation and organization of the mZIF-8 nanoparticles into micron-sized mZIF-8-rich domains within the polymer-rich phase. Upon thawing, solvent exchange, and drying, these domains are retained within the resulting polysaccharide pore walls. Consequently, mZIF-8 microspheres became embedded within the dense, solidified pore walls, while a minor fraction of individual nanoparticles remained well dispersed on the wall surface.

The resulting structure was examined by SEM, as illustrated in Fig. S8 (in ESI). Compared to the relatively smooth walls of the pristine QCS/MFC cryogel, mZIF-8@QCS/MFC-15 showed many spherical domains with diameters of approximately 1–3 μm embedded within the walls (Fig. 2a). This morphology indicates that the freezing process did not simply trap isolated nanoparticles in the network, but promoted their localized assembly into microspherical aggregates under confinement. The composition and spatial distribution of the embedded domains were further analyzed by EDS mapping. Signals from C, N, and Zn were clearly detected in the microspheres, with Zn concentrated in the interior region (Fig. 2b). This distribution supported the formation of mZIF-8-

https://doi.org/10.1007/s10118-026-3880-6

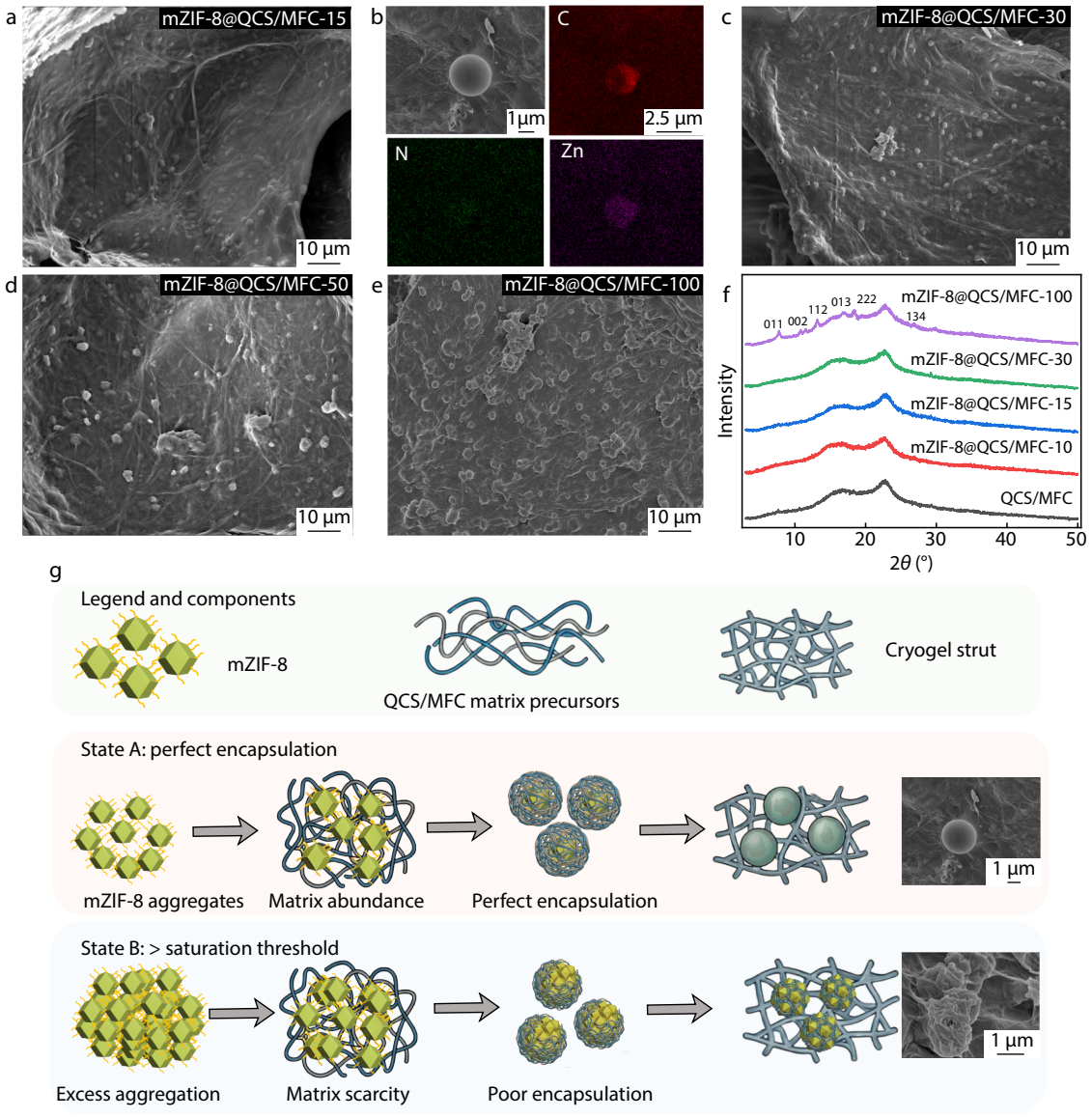


Fig. 2 Microstructural characterization of the wall-integrated mZIF-8@QCS/MFC cryogels. (a) SEM image of mZIF-8@QCS/MFC-15; (b) EDS diagrams of mZIF-8 microspheres; SEM images of (c) mZIF-8@QCS/MFC-30, (d) mZIF-8@QCS/MFC-50 and (e) mZIF-8@QCS/MFC-100; (f) XRD patterns of mZIF-8@QCS/MFC cryogels with different mZIF-8 loadings; (g) Schematic model of microsphere-in-wall formation and wall integration in the mZIF-8@QCS/MFC cryogel.

rich domains wrapped by the surrounding polysaccharide matrix. Such a configuration is beneficial because it helps mZIF-8 to remain immobilized in the wall while limiting direct exposure to the external biological environment, which is a protective feature naturally endowed by the biocompatible biomass interface.

The integrity of the wall-integrated structure depended strongly on the mZIF-8 loading. At 15 mg of loading, the microspheres were uniformly distributed, and their surfaces remained relatively smooth, suggesting effective encapsulation by the QCS/MFC matrix. When the loading was increased to 30 and 50 mg, the wall surface became rougher, and local protrusions appeared (Figs. 2c and 2d). At 100 mg, obvious crystal exposure and structural irregularities were observed, indicating that the amount of mZIF-8 exceeded the wrapping capacity of the polymer network (Fig. 2e). This evolution implies that wall integration is not only determined by the presence of mZIF-8 but also by the balance between particle assembly and polymer coverage during cryogel formation. XRD analysis further supported this interpretation (Fig. 2f). The characteristic diffraction peaks of ZIF-8 were much less pronounced in mZIF-8@QCS/MFC-15 than in the samples with higher loading, which is consistent with the stronger shielding of the crystalline phase by the polymer matrix. With increasing mZIF-8 content, the ZIF-8 peaks gradually became more distinct, especially for mZIF-8@QCS/MFC-100, reflecting the greater exposure of the crystalline component. Based on the combined morphological and structural results (Fig. 2g and Fig. S9 in ESI), mZIF-8@QCS/MFC-15 was selected as the optimized composition because it achieved a more complete

https://doi.org/10.1007/s10118-026-3880-6

microsphere-in-wall architecture while avoiding obvious crystal exposure.

Structural Characterization, Formation Mechanism, and Mechanical Properties

A hierarchical architecture was established to validate its suitability for hydrodynamic demand. As shown in Fig. 3(a), the pristine QCS/MFC cryogel exhibits an interconnected macroporous network with an average pore size of approximately 49.73 μm. After incorporating 15 mg of mZIF-8, the average pore size shifted to 48.4 μm, and the macropores remained wide open, ensuring the smooth passage of blood cells. As the mZIF-8 loading was increased to 30 mg, the average pore size gradually decreased to 44.32 μm. The pore structures of the cryogels were further evaluated by N_2 adsorption-desorption analysis. As shown in Fig. S10 and Table S1 (in ESI), the BET surface area increased from 1.13 m^2/g for QCS/MFC to 2.11 m^2/g for mZIF-8@QCS/MFC-15. At the same time, the average pore size decreased from 14.47 nm to 9.36 nm (Fig. 3b). The increase in surface area indicates that mZIF-8 contributed to an additional internal surface within the wall matrix, while the reduced pore size suggests a denser mesostructure associated with embedded microspheres. These results support a hierarchical architecture in which large pores act as transport channels and the cryogel walls provide adsorption-active domains.

As depicted in Figs. 3(c) and 3(d), FTIR and XPS analyses were employed to probe the interfacial interactions between mZIF-8 and the polysaccharide matrix. The FTIR spectra exhibit a characteristic Zn—N stretching band at 420 cm^{-1}, confirming the retention of mZIF-8.[34] Meanwhile, the —OH/—NH_2 stretching band shifts from 3346 cm^{-1} to 3390 cm^{-1}, indicating the formation of hydrogen bonds.[35] XPS further revealed diminished intensities of the N 1s peaks at 397.85 eV (—NH_2) and 401.22 eV (—NH_3^+), consistent with electrostatic interactions.[36] Collectively, these results suggest that mZIF-8 is not only physically confined, but also interacts with the surrounding QCS/MFC network, which is favorable for stable wall integration. Furthermore, XRD patterns (Fig. 2f) confirm that the crystalline integrity of mZIF-8

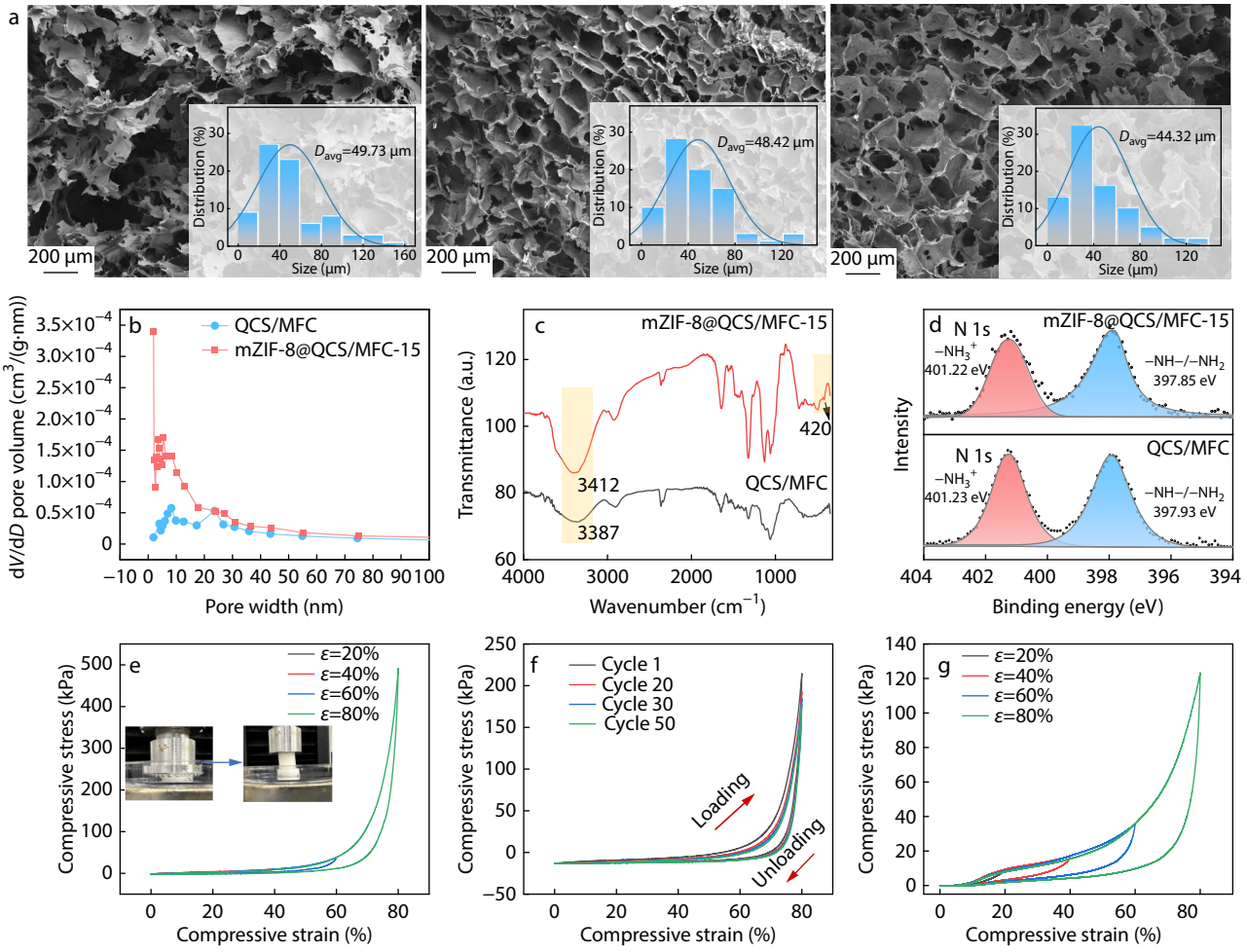


Fig. 3 Porous structure, interfacial interaction, and mechanical performance of the mZIF-8@QCS/MFC-15 cryogel. (a) SEM images of the QCS/MFC, mZIF-8@QCS/MFC-15, mZIF-8@QCS/MFC-30 and macropore size distribution of the cryogel; (b) Pore size distribution curves of QCS/MFC and mZIF-8@QCS/MFC-15 obtained from N_2 adsorption-desorption analysis; (c) FTIR spectra of QCS/MFC and mZIF-8@QCS/MFC-15 cryogels; (d) XPS spectra of QCS/MFC and mZIF-8@QCS/MFC-15 cryogels; (e) Compression-decompression stress-strain curves of mZIF-8@QCS/MFC-15 at different strains; (f) Cyclic compression behavior of mZIF-8@QCS/MFC-15 for 50 cycles at 80% strain; (g) Compression-decompression stress-strain curves of mZIF-8@QCS/MFC-15 immersed in PBS solution at 37 °C for 7 days.

was fully preserved under cryo-confinement, which was consistent with the proposed cryo-induced assembly process.

Mechanical stability is another key requirement of hemoperfusion adsorbents. Compression testing showed that mZIF-8@QCS/MFC-15 sustained a stress of 489 kPa at an 80% strain (Fig. 3e), indicating that the cryogel could resist substantial deformation. The loading-unloading curves at different strains were highly repeatable, showing good elastic recovery. In addition, the material maintained its overall shape after 50 compression cycles at 80% strain (Fig. 3f), demonstrating good fatigue resistance. Furthermore, the elastic recovery remained excellent after seven days of immersion in PBS (Fig. 3g). Such mechanical robustness is important for preserving pore architecture and preventing bed collapse under dynamic flow conditions. Thermogravimetric analysis (Fig. S11 in ESI) shows that the mZIF-8@QCS/MFC-15 cryogel exhibited a negligible mass loss of less than 2.5% in the range of 25–170 °C and no significant decomposition below 200 °C.

Bilirubin Adsorption under Albumin-containing Conditions

Because bilirubin circulates in the blood mainly in an albumin-bound state, the adsorption performance was evaluated in the presence of 40 g/L BSA as an albumin-containing model system. Although this model does not fully reproduce the complexity of authentic plasma, it provides a useful preliminary system for evaluating the albumin-bound bilirubin adsorption. Preliminary dosage experiments were conducted to determine the suitable adsorbent concentration. As shown in Fig. 4(a), increasing the dosage of mZIF-8@QCS/MFC-15 improved the bilirubin removal efficiency, but decreased the adsorption capacity calculated per unit mass. A dosage of 1.5 g/L was selected for further

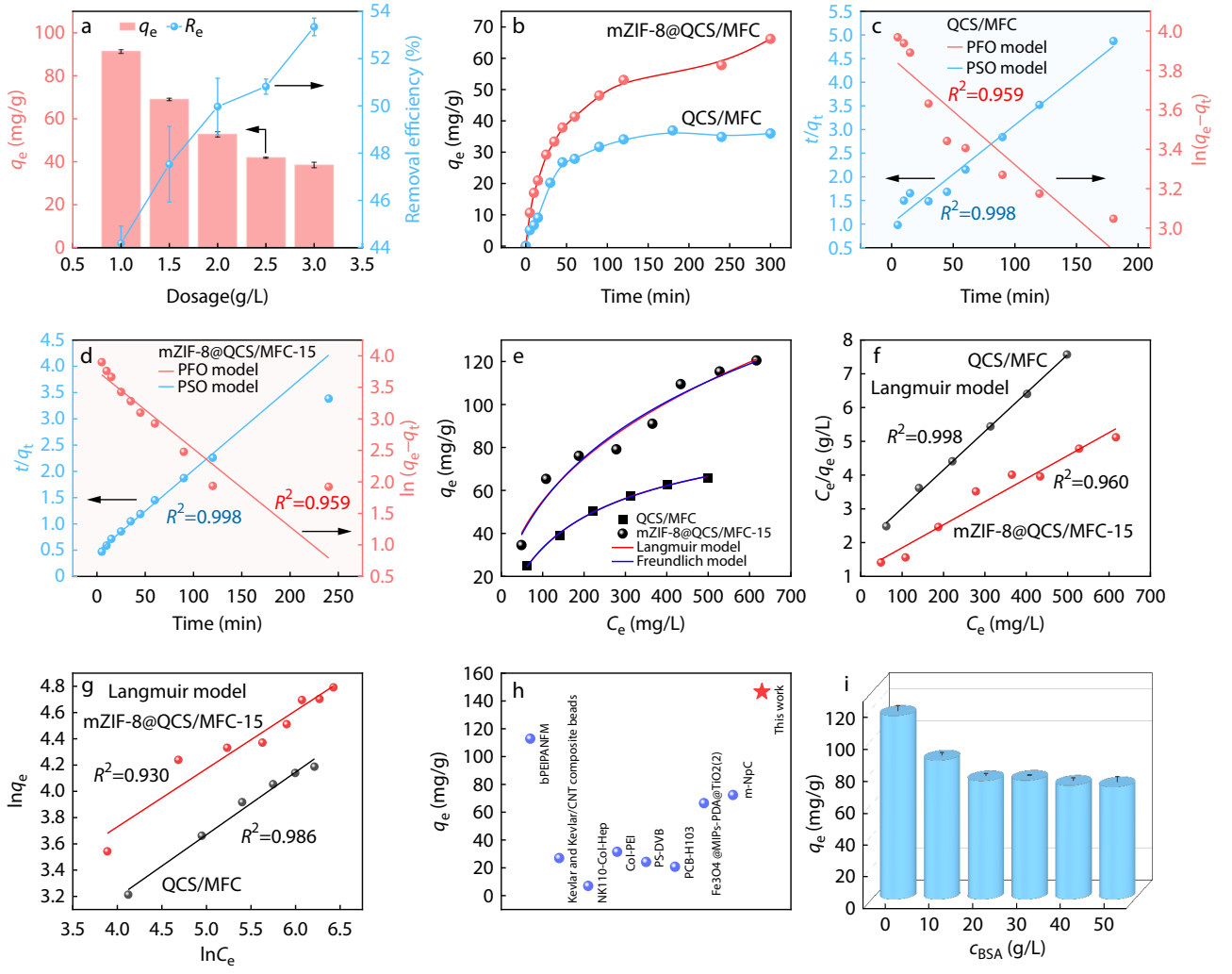


Fig. 4 Batch adsorption performance of mZIF-8@QCS/MFC-15 toward albumin-bound bilirubin. (a) Effect of adsorbent dosage on bilirubin adsorption capacity and removal efficiency in a solution containing 200 mg/L bilirubin and 40 g/L BSA; (b) Adsorption kinetic profile of mZIF-8@QCS/MFC-15 toward bilirubin in the presence of BSA; (c) Linear fitting plots of pseudo-first-order and pseudo-second-order kinetic models for QCS/MFC; (d) Linear fitting plots of pseudo-first-order and pseudo-second-order kinetic models for mZIF-8@QCS/MFC-15; (e) Adsorption isotherms of QCS/MFC and mZIF-8@QCS/MFC-15 toward bilirubin in the presence of 40 g/L BSA; (f) Nonlinear fitting of the Freundlich and Langmuir isotherm models for mZIF-8@QCS/MFC-15; (g) Linear fitting plots of the Freundlich and Langmuir isotherm models for mZIF-8@QCS/MFC-15; (h) Comparison of the bilirubin adsorption capacity of mZIF-8@QCS/MFC-15 with those of reported adsorbents; (i) Effect of BSA concentration on bilirubin adsorption by mZIF-8@QCS/MFC-15.

https://doi.org/10.1007/s10118-026-3880-6

experiments because it balanced the overall removal and adsorption efficiency.

Adsorption Kinetics

The kinetic behavior of bilirubin adsorption was studied using an initial bilirubin concentration of 200 mg/L. As shown in Fig. 4(b) and Fig. S12 (in ESI), the adsorption capacity increased rapidly at the beginning and approached equilibrium within 5 h. This relatively fast uptake indicates that bilirubin could reach the adsorption sites inside the cryogel wall without severe diffusional restriction. The combination of interconnected macroporous transport channels and wall-confined adsorption domains appeared to be favorable for maintaining adsorption accessibility. To further analyze the uptake process, the data were fitted using pseudo-first-order (PFO) and pseudo-second-order (PSO) kinetic models. The fitting plots are presented in Figs. 4(c) and 4(d), and the parameters are summarized in Table S2 (in ESI). The PSO model provided a superior fit (R^2=0.998), with a calculated equilibrium capacity (44.7 mg/g) close to the experimental value (57.8 mg/g).[37,38] This result suggests that the adsorption rate is likely governed by chemical interaction processes rather than by simple physical partitioning. This interpretation was further corroborated by the FTIR and XPS analyses presented in Section 3.6, which confirmed the specific chemical interactions between bilirubin and the mZIF-8 surface.

Adsorption Isotherms

The adsorption isotherms of bilirubin on cryogels were measured over a range of initial concentrations at 37 °C. As shown in Fig. 4(e), the adsorption capacity of the pristine QCS/MFC cryogel increased from 24.4 mg/g to 66.4 mg/g with increasing bilirubin concentration, indicating that the polysaccharide contributed to bilirubin uptake. After the incorporation of mZIF-8, the adsorption capacity increased substantially over the entire concentration range, demonstrating the positive effect of the wall-integrated MOF domains. The isotherm data were fitted using Langmuir and Freundlich models. The fitting results are shown in Figs. 4(f) and 4(g) and the corresponding parameters are listed in Table S3 (in ESI). The experimental results were best described by the Langmuir model (R^2=0.960), indicating a homogeneous monolayer adsorption.[39] The maximum adsorption capacity calculated from the Langmuir equation reached 146.6 mg/g at a dosage of 1.5 g/L and an equilibrium time of 5 h. This value compares well with those of many reported bilirubin adsorbents (Fig. 4h and Table S5 in ESI), despite the differences in experimental conditions, especially considering that the present material was tested under albumin-containing conditions. This result indicates that locating mZIF-8 within the cryogel walls did not prevent bilirubin from reaching the effective binding sites.

Effect of Albumin on Adsorption Performance

The influence of the albumin concentration on bilirubin uptake was further examined to evaluate the selectivity of the cryogel under competitive conditions. As shown in Fig. 4(i), the bilirubin adsorption capacity gradually decreased as the BSA concentration increased, which was consistent with the stronger association between bilirubin and albumin at higher protein levels. Nevertheless, more than 50% of the adsorption capacity measured in the absence of BSA was retained, even at 50 g/L BSA, indicating that the adsorbent remained active under physiologically relevant protein concentrations. To further evaluate protein loss during bilirubin adsorption, competitive adsorption analysis was performed. During the adsorption process, the bilirubin concentration decreased by 41.9% within 300 min, whereas the BSA concentration decreased by only 3.84% over the same period (Fig. S12 in ESI), corresponding to a BSA retention of 96.16%. Direct BSA adsorption experiments also showed a limited protein uptake by the composite cryogel (Fig. S13 in ESI). These results indicated that bilirubin uptake was more pronounced than nonspecific BSA adsorption under the tested model conditions. This selectivity can be attributed to the wall-integrated structure. The hydrophilic QCS/MFC walls may suppress nonspecific contact between albumin and the mZIF-8 domains, whereas the large size of albumin limits its penetration into the microporous framework. Under these conditions, bilirubin can still be transferred from albumin to high-affinity sites within the cryogel walls.

Dynamic Adsorption by Simulated Hemoperfusion Devices

To evaluate the adsorption behavior under flow conditions, mZIF-8@QCS/MFC-15 was packed into a fixed-bed column and tested in a simulated hemoperfusion setup (Fig. 5a). The albumin-bound bilirubin solution was continuously pumped through the column, and the breakthrough behavior was analyzed using the Thomas and Yoon-Nelson models.[40] Dynamic testing is particularly important for this material because the wall-integrated design is intended not only to adsorb bilirubin but also to maintain structural integrity and open transport channels under perfusion conditions.

As shown in Figs. 5(b)–5(e) and Fig. S14 (in ESI), both models described the experimental breakthrough curves reasonably well, and the Thomas model provided a particularly good fit. The fitted parameters are summarized in Table S4 (in ESI). The agreement between the experimental and fitted curves indicates that the adsorption behavior under flow conditions can be interpreted in terms of the commonly used fixed-bed adsorption kinetics. When the column length was fixed at 9 cm, increasing the flow rate from 1 mL/min to 3 mL/min reduced the equilibrium adsorption capacity from 26.7 mg/g to 20.9 mg/g. This trend reflects the shorter residence time at higher flow rates, which limits the mass transfer from the flowing solution to the adsorption sites located within the cryogel wall. In contrast, when the flow rate was maintained at 3 mL/min, increasing the column length from 3 cm to 12 cm increased the equilibrium adsorption capacity from 16.5 mg/g to 22.4 mg/g. A longer bed increases the contact time and available adsorption volume, thereby improving bilirubin capture. The Yoon-Nelson fitting showed a similar tendency. When the bed depth increased from 3 cm to 12 cm, the processed volume at 50% breakthrough increased from 17.1 mL to 75.0 mL, indicating improved dynamic treatment capacity. Throughout the test, the cryogel column maintained a stable flow behavior without obvious compaction or disintegration. This result is consistent with the mechanical data and suggests that the resultant cryogel can tolerate shear and compression conditions associated with continuous perfusion.

While the BSA-bilirubin competitive system is widely adopted as the standard model for evaluating bilirubin

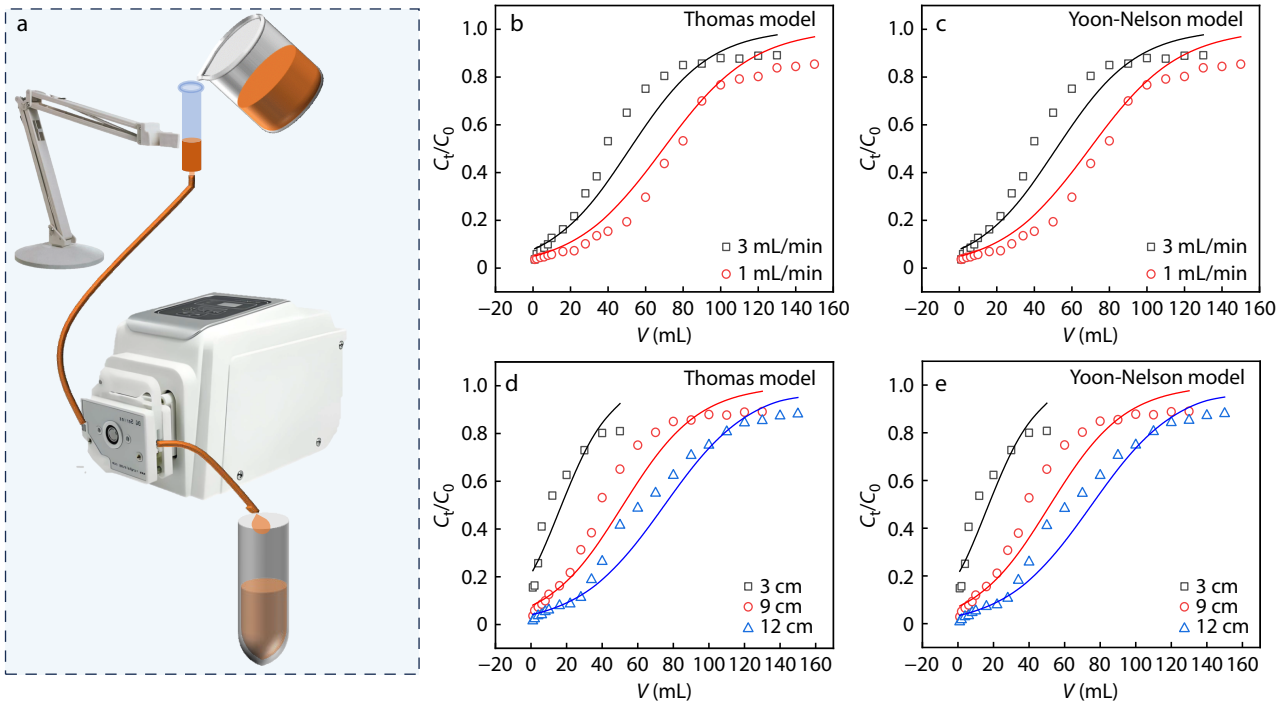


Fig. 5 Dynamic bilirubin adsorption performance of mZIF-8@QCS/MFC-15 in a simulated hemoperfusion system. (a) Photograph of the fixed-bed adsorption device used for continuous-flow testing; (b, c) Experimental and fitted breakthrough curves for bilirubin adsorption from albumin-containing solution at different flow rates based on the Thomas model and Yoon-Nelson model, respectively; (d, e) Experimental and fitted breakthrough curves for bilirubin adsorption from albumin-containing solution at different column lengths based on the Thomas model and Yoon-Nelson model, respectively.

hemoperfusion applicability,[15,35,41–43] physiological environments introduce further complexities, such as electrolyte competition and competitive binding from globulins or other uremic toxins. Although this work focuses on the novel "microsphere-in-wall" architecture and its adsorption mechanisms, preclinical validation in human plasma and *in vivo* animal models should be conducted to bridge this gap toward clinical translation. In particular, long-term hemocompatibility, preservation of essential plasma proteins, material stability, potential component leakage, sterilization, and *in vivo* safety should be systematically evaluated before clinical application.

Adsorption Mechanism

To clarify the binding mechanism of bilirubin, mZIF-8@QCS/MFC-15 was analyzed before and after adsorption using FTIR and XPS. In the FTIR spectra, the band at 1644 cm^{-1} shifted to 1653 cm^{-1} after bilirubin adsorption (Fig. 6a), which indicates changes in the local chemical environment of the carbonyl- and amino-related groups.[44] In addition, the broad O—H and N—H stretching bands shifted from 3390 cm^{-1} to 3416 cm^{-1}, suggesting that hydrogen bonding interactions were altered after bilirubin binding.[45]

XPS analysis provided further evidence of adsorption. After bilirubin uptake, new C 1s signals appeared at 288.01 and 288.99 eV, corresponding to C=O and O—C=O species, respectively (Fig. 6b), which are consistent with the presence of bilirubin-derived chemical groups on the adsorbent surface.[24] At the same time, the N 1s spectrum showed a decrease in the protonated amino component and a shift in the amino-related peak, indicating the involvement of nitrogen-containing groups in the adsorption process.[46,47] Based on these results, bilirubin capture by the composite cryogel can be described as a cooperative process involving both the polysaccharide matrix and the embedded mZIF-8 domains (Fig. 6c). The positively charged QCS can help attract bilirubin species and enrich them near the cryogel wall, whereas mZIF-8 provides stronger local binding through hydrogen bonding and related short-range interactions. Therefore, the cryogel wall acts not only as a support for immobilizing the MOF but also as an active interfacial region that participates in the capture of bilirubin.

Blood Compatibility and Cytotoxicity Testing

For a blood-contacting adsorbent, good hemocompatibility is as important as the adsorption performance. The hemolysis ratio of mZIF-8@QCS/MFC-15 was measured according to ASTM F756-2008. As shown in Fig. 7(a), the hemolysis ratio was 0.4%, which is well below the 5% threshold commonly used to define nonhemolytic materials.[48,49] This result indicates that the cryogel caused minimal damage to blood cells under the test conditions. The low hemolysis may be related to the hydrophilic polysaccharide interface and limited direct exposure of mZIF-8 to the wall-integrated structure.

Coagulation-related behavior was evaluated by measuring the APTT, PT, and TT (Fig. 7b). Compared with the control, the APTT increased slightly from 29.9 s to 33.3 s, while PT and TT remained largely unchanged. These results suggested that the cryogel did not strongly disturb the coagulation cascade *in vitro*. Although a modest prolongation of APTT was observed, the overall coagulation profile remained stable, which is favorable for further consideration in blood purification ap-

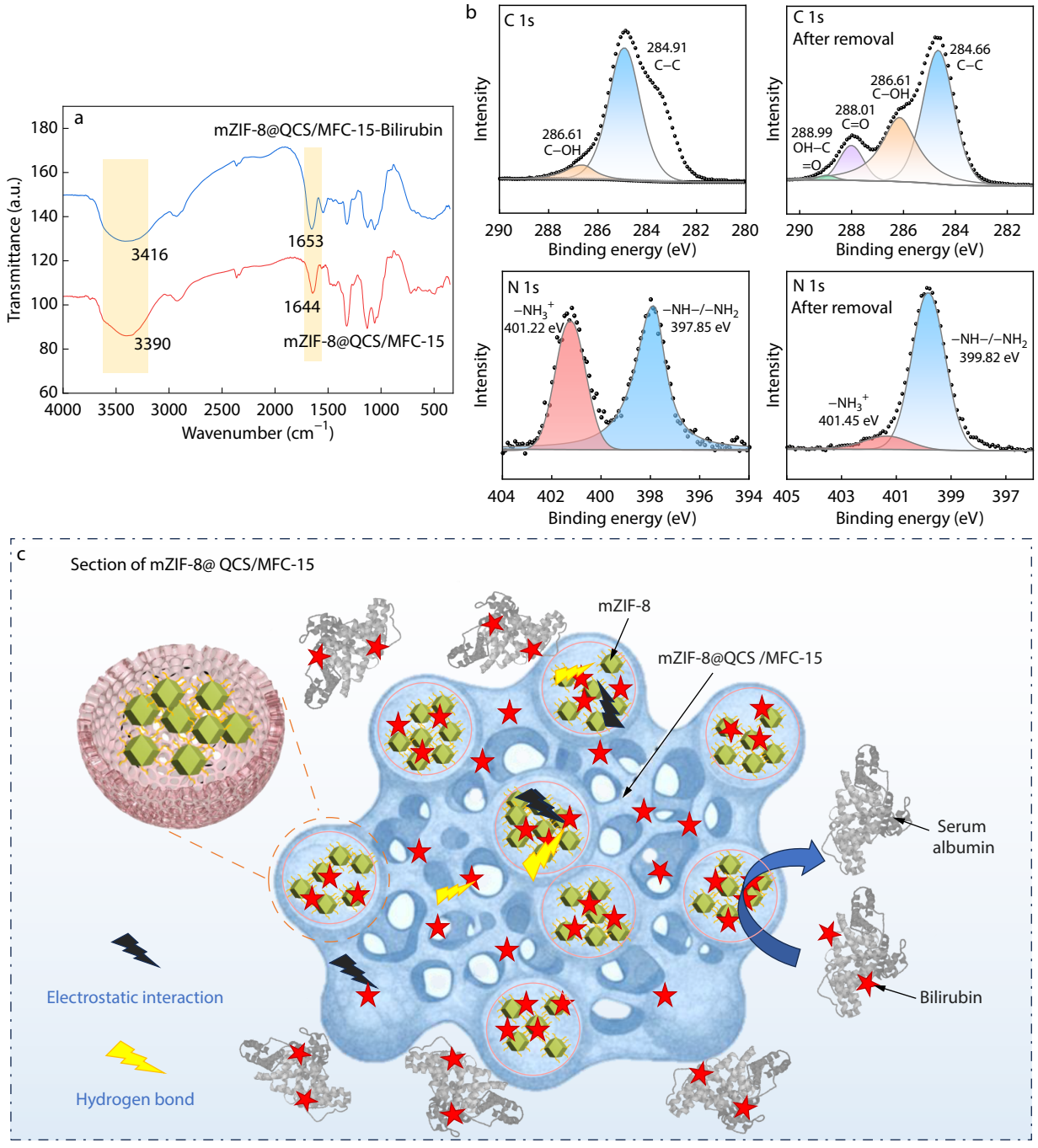


Fig. 6 Spectroscopic analysis of the bilirubin adsorption mechanism of mZIF-8@QCS/MFC-15. (a) FTIR spectra of mZIF-8@QCS/MFC-15 before and after bilirubin adsorption; (b) XPS spectra of mZIF-8@QCS/MFC-15 before and after bilirubin adsorption; (c) Schematic illustration of the cooperative bilirubin adsorption mechanism involving the QCS/MFC wall and wall-confined mZIF-8 domains.

plications.

Cytocompatibility was assessed using HUVECs and the sample extracts. As shown in Fig. 7(c), cell viability remained close to 100% even at an extract concentration of 1.5 g/L, indicating that no obvious cytotoxic effects were detected. Live-dead staining yielded consistent results, with most cells remaining viable after exposure to the extract (Fig. 7d). These observations suggested that the composite cryogel did not release significant amounts of harmful components under the tested conditions. Taken together, the blood compatibility and cytocompatibility results support the utility of wall-integrated design for developing safer biomass-based hemoperfusion materials.

To ensure clinical safety, we evaluated the potential leakage of Zn^{2+} and mZIF-8 particles under simulated physiological conditions. mZIF-8@QCS/MFC-15 cryogel was immersed in PBS (pH=7.4) at 37 °C for 48 h with continuous agitation. As shown in Fig. S15 (in ESI), the solution remained clear with no observable particles after soaking. The supernatant was analyzed using ICP-MS. The Zn^{2+} concentration remained below

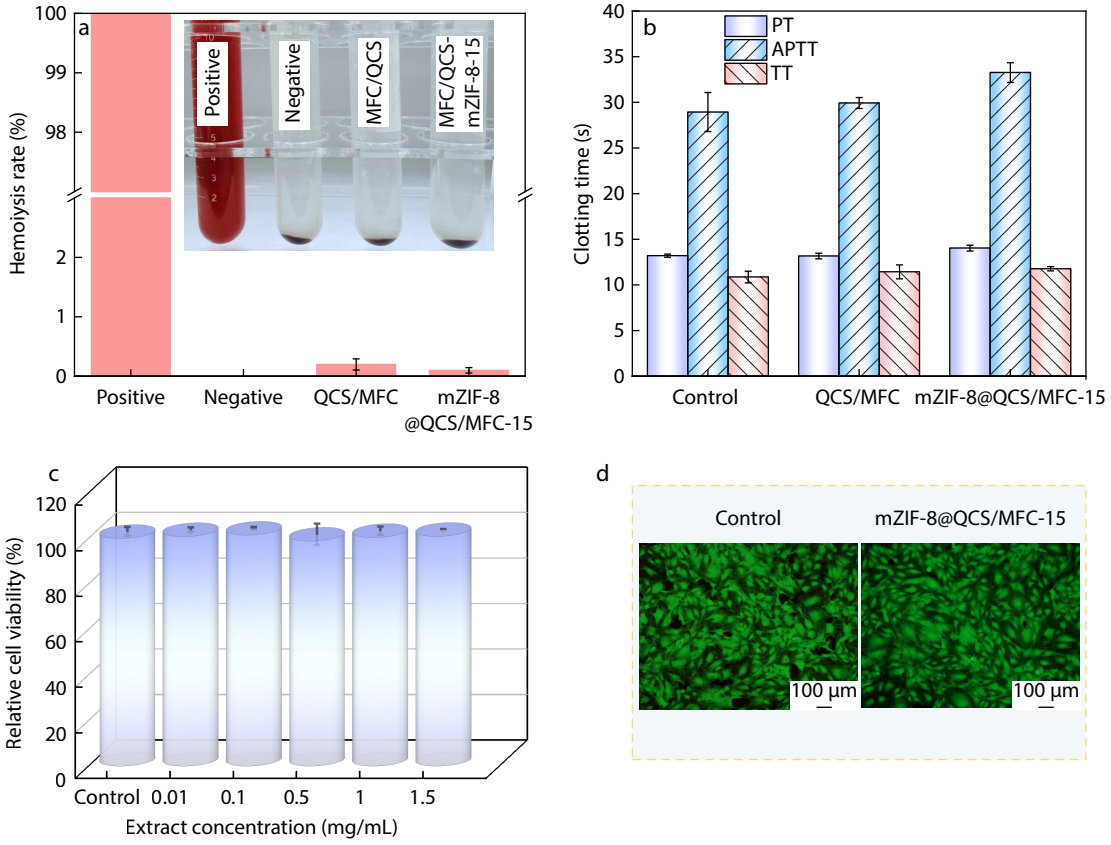


Fig. 7 Hemocompatibility and cytocompatibility of the cryogel adsorbents. (a) Hemolysis ratios of QCS/MFC and mZIF-8@QCS/MFC-15; (b) Coagulation parameters including activated partial thromboplastin time, prothrombin time, and thrombin time; (c) Cell viability of HUVECs after incubation with cryogel extracts at different concentrations. Data are presented as mean ± standard deviation for three independent measurements. (d) Fluorescence images of HUVECs stained with AM/PI after treatment with cryogel extracts, where green indicates live cells and red indicates dead cells.

0.23 μg/mL, which was well within the safety standards for blood-contacting materials.[50,51]

CONCLUSIONS

A wall-integrated mZIF-8@QCS/MFC cryogel was constructed using a cryo-induced assembly process for bilirubin hemoperfusion. During freezing, amino-functionalized ZIF-8 nanoparticles were concentrated in polymer-rich interstitial regions, where they assembled into microspheres and became confined within the QCS/MFC cryogel walls. This process generates a microsphere-in-wall architecture that combines open macroporous channels for fluid transport, with adsorption-active wall domains for bilirubin capture. The optimized composite cryogel exhibited a bilirubin saturation capacity of 146.6 mg/g in albumin-containing solution. Spectroscopic analysis indicated that bilirubin uptake is associated with the combined action of the positively charged polysaccharide matrix and mZIF-8, involving electrostatic attraction and hydrogen bonding. The QCS/MFC wall also played a critical interfacial role by limiting the direct exposure of mZIF-8 to the external environment, which was consistent with the low hemolysis ratio of 0.4% and stable coagulation profile observed *in vitro*. In addition, the cryogel maintained its structural integrity and adsorption function under simulated continuous-flow conditions, indicating its potential as a perfusion-type bilirubin adsorbent. This study demonstrated that the spatial organization of MOF particles within carbohydrate cryogel walls is key to improving the balance between adsorption accessibility and biological safety. In the present system, the polysaccharide wall acted not only as a supporting scaffold but also as a functional interface that contributed to particle immobilization, selective accessibility, and blood compatibility. Although the current evaluation was mainly conducted using albumin-containing model solutions, the results provide a useful basis for further studies in more complex plasma systems and animal models. Overall, microsphere-in-wall design provides a useful structural strategy for developing biomass-based adsorbents for albumin-bound bilirubin removal.

Conflict of Interests

The authors declare no interest conflict.

Electronic Supplementary Information

Electronic supplementary information (ESI) is available free of charge in the online version of this article at http://doi.org/10.1007/s10118-026-3880-6.

ACKNOWLEDGMENTS

The work was financially supported by the Reserve Talents Project for Youth and Middle Aged Academic and Technical Leaders of Yunnan Province (No. 202205AC160032), the National Natural Science Foundation of China (Nos. 52663014 and 52503145), and the Yunnan Provincial Graduate Supervisor Team Construction Project (2024).

REFERENCES

1 Yang, Y.; Yin, S.; He, C.; Wu, X.; Yin, J.; Zhang, J.; Ma, L.; Zhao, W.; Cheng, C.; Zhao, C. Construction of kevlar nanofiber/graphene oxide composite beads as safe, self-anticoagulant, and highly efficient hemoperfusion adsorbents. *J. Mater. Chem. B* **2020**, *8*, 1960–1970.

2 Wu, K.; Liu, X.; Li, Z.; Jiao, Y.; Zhou, C. Fabrication of chitosan/graphene oxide composite aerogel microspheres with high bilirubin removal performance. *Mater. Sci. Eng. C* **2020**, *106*, 110162.

3 Liu, Y.; Wang, Z. K.; Liu, C. Z.; Liu, Y. Y.; Li, Q.; Wang, H.; Cui, F.; Zhang, D. W.; Li, Z. T. Supramolecular organic frameworks as adsorbents for efficient removal of excess bilirubin in hemoperfusion. *ACS Appl. Mater. Interfaces* **2022**, *14*, 47397–47408.

4 Moreau, R.; Gao, B.; Papp, M.; Bañares, R.; Kamath, P. S. Acute-on-chronic liver failure: a distinct clinical syndrome. *J. Hepatol.* **2021**, *75*, S27–S35.

5 Song, X.; Xu, T.; Yang, L.; Li, Y.; Yang, Y.; Jin, L.; Zhang, J.; Zhong, R.; Sun, S.; Zhao, W.; Zhao, C. Self-anticoagulant nanocomposite spheres for the removal of bilirubin from whole blood: a step toward a wearable artificial liver. *Biomacromolecules* **2020**, *21*, 1762–1775.

6 Wu, S.; Yue, P.; Ma, Y.; Zou, Y.; Liang, W.; Ye, Q. Hemoperfusion adsorbents for removal of common toxins in liver and kidney failure: recent progress, challenges, and prospects. *Adv. Mater.* **2025**, *37*, 2305152.

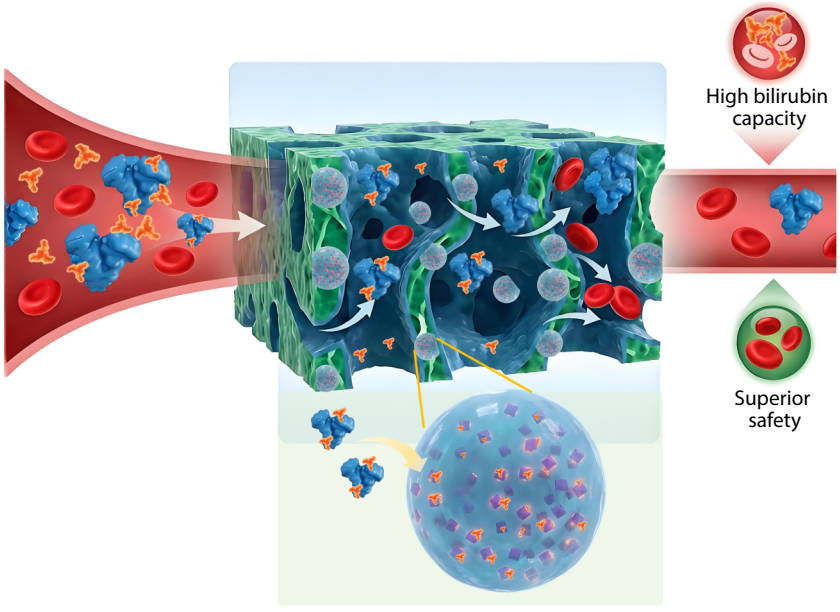
Graphical Abstract

Cryo-induced Encapsulation of Amino-functionalized Zeolitic Imidazolate Framework-8 Microspheres within Biomass-based Cryogel Walls for Effective Hemoperfusion

Pei-Rong Jiang, Xu-Feng Zhang, Ji-Ping Weng, Yan Liu, Jin Huang, Xiang-Yu Chen, Jing Shen, Xi-Yun Feng, Liang-Fei Duan, and Jun Wang

Yunnan Normal University; Shihezi University; Southwest Hospital of Army Medical University

A "microsphere-in-wall" architecture integrated amino-functionalized zeolitic imidazolate framework-8 (mZIF-8) into biomass cryogels *via* cryo-induced assembly. This spatial confinement ensures the highly efficient capture of albumin-bound bilirubin while shielding blood cells from direct metal-organic framework (MOF) contact, successfully balancing the adsorption capacity with excellent hemocompatibility.



Chinese J. Polym. Sci. 2026 *https://doi.org/10.1007/s10118-026-3880-6*

7 Yin, H. X.; Xiao, Y. Y.; Cai, Y. C.; He, S. L.; Wang, Y.; Zhang, G. S.; Zhang, C.; Tan, B. E.; Hussain, I.; Yan, W. Ionic hyper crosslinked polymers as high performance hemoperfusion adsorbent for efficient removal of excessive bilirubin. *Chinese J. Polym. Sci.* **2026**, *44*, 154–161.
8 Li, J.; Han, L.; Xie, J.; Liu, S.; Jia, L. Multi-sites polycyclodextrin adsorbents for removal of protein-bound uremic toxins combining with hemodialysis. *Carbohydr. Polym.* **2020**, *247*, 116665.
9 Li, M.; Wang, X.; Gong, G.; Li, X.; Tang, Y.; Wang, Q.; Zhou, J.; Guo, J.; Liao, X.; Shi, B. Engineered liver-inspired collagen matrix as a high-performance hemoperfusion adsorbent for bilirubin removal. *Chem. Eng. J.* **2021**, *426*, 130791.
10 Wang, Y.; Zhou, X.; Yang, X.; Liang, J.; Chen, S.; Ling, Z.; Wang, W.; Shao, Z.; Song, X.; Wei, R.; Zhao, W.; Zhao, C. Strategic nanoarchitectonics of porous beads for protein-bound toxin removal with self-photodecomposition and visual monitoring for hyperbilirubinemia. *Adv. Funct. Mater.* **2025**, *35*, 2502795.
11 Feng, X.; Li, J.; Peng, Y.; Guo, W.; Liang, L.; Zhu, L.; Liu, S.; Ren, L. Zwitterionic polymers as high-performance coatings for hemoperfusion adsorbents and their chemisorption of protein-bound toxins through computational simulations. *Colloids Surf. A Physicochem. Eng. Asp.* **2024**, *680*, 132710.
12 Zhao, R.; Ma, T.; Cui, F.; Tian, Y.; Zhu, G. Porous aromatic framework with tailored binding sites and pore sizes as a high-performance hemoperfusion adsorbent for bilirubin removal. *Adv. Sci.* **2020**, *7*, 2001899.
13 Zhang, M.; Wang, Y.; Zhou, W.; Zheng, X.; Liu, X.; Zhu, B.; Wang, S.; Zhou, L. Ordered mesoporous SiO_2 as hemoperfusion adsorbents for enhanced selectivity of bilirubin removal from blood. *Sep. Purif. Technol.* **2025**, *359*, 130640.
14 Dou, W.; Wang, J.; Yao, Z.; Xiao, W.; Huang, M.; Zhang, L. A critical review of hemoperfusion adsorbents: materials, functionalization and matrix structure selection. *Mater. Adv.* **2022**, *3*, 918–930.
15 Zhou, W.; Zhang, M.; Liu, X.; Hussain, W.; Zhu, B.; Yu, H.; Wang, S.; Zhou, L. Collagen-modified chitosan microsphere as a novel hemoperfusion adsorbent for efficient removal of bilirubin from human plasma. *Sep. Purif. Technol.* **2024**, *337*, 126303.
16 Chai, Y.; Liu, Z.; Du, Y.; Wang, L.; Lu, J.; Zhang, Q.; Han, W.; Wang, T.; Yu, Y.; Sun, L.; Ou, L. Hydroxyapatite reinforced inorganic-organic hybrid nanocomposite as high-performance adsorbents for bilirubin removal *in vitro* and in pig models. *Bioact. Mater.* **2021**, *6*, 4772.
17 Zhou, W.; Hu, W.; Zhan, Q.; Zhang, M.; Liu, X.; Hussain, W.; Yu, H.; Wang, S.; Zhou, L. Novel hemoperfusion adsorbents based on collagen for efficient bilirubin removal-a thought from yellow skin of patients with hyperbilirubinemia. *Int. J. Biol. Macromol.* **2023**, *253*, 127321.
18 Chen, J.; Ma, Y.; Wang, L.; Han, W.; Chai, Y.; Wang, T.; Li, J.; Ou, L. Preparation of chitosan/SiO_2-loaded graphene composite beads for efficient removal of bilirubin. *Carbon* **2019**, *143*, 352–361.
19 Mo, Z.; Tai, D.; Zhang, H.; Shahab, A. A comprehensive review on the adsorption of heavy metals by zeolite imidazole framework (ZIF-8) based nanocomposite in water. *Chem. Eng. J.* **2022**, *443*, 136320.
20 Ahmad, W.; Tahir, M.; Bibi, B.; Gong, F.; He, L.; Tang, H.; Qu, L.; Nisa, F. U.; Naseem, M.; Ullah, H.; Manzoor, S.; Chen, J.; Zhang, K.; Peng, Z.; Ma, Z.; Khan, A. U.; Xiong, Y.; Sabir, M.; Tang, X.; Dai, J. Advances in ZIF-8 variants: synthesis, design, and applications in gas sensing. *Coord. Chem. Rev.* **2025**, *539*, 216733.
21 Jiang, X.; Zhou, D.; Huang, X.; Zhao, W.; Zhao, C. Hexanediamine functionalized poly(glycidyl methacrylate-co-N-vinylpyrrolidone) particles for bilirubin removal. *J. Colloid Interface Sci.* **2017**, *504*, 214–222.
22 Liu, Y.; Yuan, Z.; Chen, Y. Metal–organic framework (UiO-66 and UiO-66-NH_2)-based adsorbents for bilirubin removal used in hemoperfusion. *RSC Adv.* **2023**, *13*, 35078–35087.
23 Wang, W.; Zhang, H.; Zhang, Z.; Luo, M.; Wang, Y.; Liu, Q.; Chen, Y.; Li, M.; Wang, D. Amine-functionalized PVA-co-PE nanofibrous membrane as affinity membrane with high adsorption capacity for bilirubin. *Colloids Surf. B Biointerfaces* **2017**, *150*, 271–278.
24 Gan, N.; Sun, Q.; Peng, X.; Ai, P.; Wu, D.; Yi, B.; Xia, H.; Wang, X.; Li, H. MOFs-alginate/polyacrylic acid/poly(ethylene imine) heparin-mimicking beads as a novel hemoadsorbent for bilirubin removal *in vitro* and *vivo* models. *Int. J. Biol. Macromol.* **2023**, *235*, 123868.
25 Li, Q.; Guo, H.; Yang, J.; Zhao, W.; Zhu, Y.; Sui, X.; Xu, T.; Zhang, J.; Zhang, L. MOF-based antibiofouling hemoadsorbent for highly efficient removal of protein-bound bilirubin. *Langmuir* **2020**, *36*, 8753–8763.
26 Hu, Z.; He, F.; Liu, A.; Shao, R.; You, J.; Wu, S.; Zhao, X.; Ye, Q.; Shi, X.; Zhong, Z. Engineering a biocompatible chitosan/MOF aerogel for hyperbilirubinemia treatment in liver failure. *J. Mater. Chem. B* **2025**, *13*, 11210–11223.
27 Bao, C.; Zhang, X.; Shen, J.; Li, C.; Zhang, J.; Feng, X. Freezing-triggered gelation of quaternized chitosan reinforced with microfibrillated cellulose for highly efficient removal of bilirubin. *J. Mater. Chem. B* **2022**, *10*, 8650–8663.
28 Jiang, P.; Kong, L.; Feng, X.; Wang, J.; Duan, L.; Shen, J.; Zhang, L.; Zhang, X. Multisite adsorption of de novo engineered zeolitic imidazolate framework for efficient removal of organic pollutants. *J. Environ. Chem. Eng.* **2026**, *14*, 121956.
29 Zhou, L.; Li, N.; Jin, X.; Owens, G.; Chen, Z. A new nFe@ZIF-8 for the removal of Pb(II) from wastewater by selective adsorption and reduction. *J. Colloid Interface Sci.* **2020**, *565*, 167–176.
30 Chen, F.; Liu, S.; Huang, H.; Wang, B.; Liu, Z.; Jiang, X.; Xiang, W.; Yang, G.; Liu, G.; Peng, X.; Zhang, Z.; Liu, Z.; Tsubaki, N. Fast synthesis of Cu@zeolitic imidazolate framework-8 (ZIF-8) derived Cu/ZnO catalysts *via* a facile mechanical grinding method for CO_2 hydrogenation to methanol. *Chem. Sci.* **2025**, *16*, 2273–2286.
31 Zhong, W.; Wang, N.; Huang, F.; Nie, B.; Lei, Y.; Qin, W.; Tiwari, S. K.; Ola, O.; Wang, X.; Zhu, Y. Rational design of heterostructured MOF-on-MOF (NH_2-MIL-125(Ti)@ZIF-8) nanocomposites with synergistic ion-exchange for efficient cesium sequestration in wastewater treatment. *Chem. Eng. J.* **2025**, *522*, 166789.
32 Li, M.; Chen, J.; Tuo, Y.; Huang, C.; Ge, Y.; Li, Z. Regulating defect sites and active groups in ZIF-8 with 5-amino-1H-tetrazole *via* solvent-assisted linker exchange enables superior pollutant removal in wastewater. *Chem. Eng. J.* **2025**, *508*, 160671.
33 Wang, T.; Wang, Y.; Sun, M.; Hanif, A.; Wu, H.; Gu, Q.; Ok, Y. S.; Tsang, D. C. W.; Li, J.; Yu, J.; Shang, J. Thermally treated zeolitic imidazolate framework-8 (ZIF-8) for visible light photocatalytic degradation of gaseous formaldehyde. *Chem. Sci.* **2020**, *11*, 6670–6681
34 Li, K.; Chen, M.; Chen, L.; Zhao, S.; Pan, W.; Li, P.; Han, Y. Adsorption of tetracycline from aqueous solution by ZIF-8: isotherms, kinetics and thermodynamics. *Environ. Res.* **2024**, *241*, 117588.
35 Guo, C.; Gao, J.; Wang, C.; Wu, S.; Chang, C. Surface engineering of cellulose microspheres *via* amyloid-like protein aggregation for bilirubin removal. *Carbohydr. Polym.* **2025**, *368*, 124145.
36 Cui, Y.; Zhang, X.; Chen, G.; Liu, K.; Meng, H.; Shen, J.; Wang, J.; Feng, X. Microfibrillated cellulose reinforced polyethyleneimine cryogels fabricated *via* cryo-induced chemical crosslinking for enhanced removal of albumin-bound bilirubin. *Int. J. Biol. Macromol.* **2025**, *306*, 141595.
37 Kou, X.; Huang, Y.; Yang, Y. Effect of the length and aromaticity of N_3-substituent on adsorption performance of imidazolium-based poly(ionic liquids) towards Pd(II). *J. Hazard. Mater.* **2021**, *420*,

126623.
38 Wang, Y.; Wang, S.; He, X.; Li, Y.; Xu, T.; Xu, L.; Yang, B.; Fan, X.; Zhao, W.; Zhao, C. A breakthrough trial of an artificial liver without systemic heparinization in hyperbilirubinemia beagle models. *Bioact. Mater.* **2023**, *20*, 651–662.
39 Deng, N.; Jin, L.; Peng, J.; Chen, S.; Ling, Z.; Liu, X.; Wang, J.; Yin, J.; Su, B.; Zhao, W.; Zhao, C. Imidazole-functionalized quaternary ammonium salts modified polyether sulfone microspheres for highly efficient bilirubin removal in whole blood. *Adv. Healthc. Mater.* **2025**, *15*, e03176.
40 Zhao, Q.; Seredych, M.; Precetti, E.; Shuck, C. E.; Harhay, M.; Pang, R.; Shan, C.-X.; Gogotsi, Y. Adsorption of uremic toxins using Ti_3C_2Tx MXene for dialysate regeneration. *ACS Nano* **2020**, *14*, 11787–11798.
41 Zhou, W.; Yu, H.; Zhu, B.; Zhang, M.; Liu, X.; Wang, H.; Wang, S.; Zhou, L. Collagen and heparin co-modification of NK110 microspheres for enhanced bilirubin adsorption and improved blood compatibility in hemoperfusion. *Sep. Purif. Technol.* **2025**, *372*, 133541.
42 Huang, S.; Zheng, J.; Zhang, Y.; Zheng, J.; Zhuang, Z.; Yang, Q.; Wang, F.; Chen, G.; Huang, S.; Ouyang, G. Polydopamine decorated ordered mesoporous carbon for efficient removal of bilirubin under albumin-rich conditions. *J. Mater. Chem. B* **2020**, *8*, 290–297.
43 Li, K.; Wang, C.; Gao, Y.; Xu, B.; Zhao, X.; Xu, Z.; Hou, M.; Qi, R.; Gan, J.; Huang, Y.; Yang, M.; Zhao, M.; Zhuang, D.; Li, Y.; Gong, Q. Preparation of zwitterion-decorated carbon nanotubes/ZIF-8 composite aerogel beads as an effective adsorbent for protein-bound uremic toxins removal in hemoperfusion. *Carbon* **2025**, *244*, 120689.
44 Gan, N.; Li, Y.; Liu, P.; Pang, J.; Chen, L.; Geng, F.; Li, H.; Wu, D. Experimental and computational investigations of Zirconium-based metal-organic frameworks for bilirubin adsorption. *Microporous Mesoporous Mater.* **2024**, *369*, 113054.
45 Diejomaoh, O. T. A.; Lavoratti, A.; Laverock, J.; Koev, T. T.; Khimyak, Y. Z.; Kondo, T.; Eichhorn, S. J. Surface modification of cellulose nanomaterials with amine functionalized fluorinated ionic liquids for hydrophobicity and high thermal stability. *Carbohydr. Polym.* **2024**, *344*, 122519.
46 Feng, J.; Huang, D.; Hu, J.; Li, J.; Zhang, J.; Fu, H.; Chang, J.; Gao, H.; Liao, Y. BSA-grafted porous amino polypyrrole for efficient removal of excess bilirubin in hemoperfusion. *Eur. Polym. J.* **2023**, *200*, 112550.
47 Wang, Y.; Li, C.; Zheng, Y.; Xie, Y.; Qiao, K.; He, W.; Yang, S. Plant protein modified natural cellulose with multiple adsorption effects used for bilirubin removal. *Int. J. Biol. Macromol.* **2021**, *166*, 179–189.
48 Wang, X.; Yu, M.; Kamal Hadi, M.; Niu, J.; Zhang, Y.; Zhou, Q.; Ran, F. An anticoagulant supercapacitor for implantable applications. *Nat. Commun.* **2024**, *15*, 10497.
49 Teng, L.; Shao, Z. W.; He, Y. S.; Lu, J. Y.; Zou, D. R.; Feng, C. L.; Dong, C. M. A glycosylated and catechol-crosslinked ε-polylysine hydrogel: simple preparation and excellent wound hemostasis and healing properties. *Chinese J. Polym. Sci.* **2022**, *40*, 1110–1119.
50 Singh, N.; Qutub, S.; Khashab, N. M. Biocompatibility and biodegradability of metal organic frameworks for biomedical applications. *J. Mater. Chem. B* **2021**, *9*, 5925–5934.
51 Abbas, M.; Liang, Z.; Chen, M.; Qu, W.; Khan, S.; Ashaq, M. S.; Chen, D.; Xie, S. Toxicity challenges and current advancement in metal-organic frameworks (MOFs) for biomedical applications. *Biol. Trace Elem. Res.* **2025**, *204*, 836–852.